Investigation of Structural Stability, Morphology, and Optical Properties of Lead Sulfide Quantum Dots Under the Influence of Acoustic Shock Waves

R. Yoga Indra Eniya[1], K. Vijaykumar[1], F. Irine Maria Bincy[2] and B. Vigneashwari[1,*]

[1]*Department of Physics, Government Arts College for Men, Krishnagiri, Tamil Nadu, India*

[2]*Shock Wave Research Laboratory, Department of Physics, Abdul Kalam Research Center, Sacred Heart College (Autonomous), Tirupattur, affiliated to Thiruvalluvar University, Tamil Nadu, 635 601, India*

Abstract: Lead sulfide (PbS), due to its high performance, is an interesting semiconducting material for solar cell applications. In this study, the synthesis of PbS by the co-precipitation route was adopted due to a low-cost synthesis procedure. The powder X-ray diffraction (PXRD) technique and Rietveld refinement revealed PbS with a face-centered cubic structure. The optical properties are widely studied using absorption and photoluminescence studies. To check the stability of the sample under high-pressure conditions, acoustic shock waves are imposed on the PbS NPs, and their stability is analyzed under various shockwave-loaded conditions. The impact of acoustic shock waves upon the quantum dots (QDs) is one of the fascinating ideas for active research in material science. The stability of PbS QDs was examined through multiple characterization techniques such as PXRD, HRTEM, SAED, FESEM, EDAX, UV-Visible-NIR spectroscopy, and photoluminescence (PL) for shock-exposed conditions. Our findings reveal that PbS QDs show no significant changes in crystallographic structure and showcase the possibility of bandgap tuning under the high-pressure acoustic shockwaves of 0.59 MPa in the counts of 200 & 400 shock pulses with a 1.5 Mach number. PbS QDs show shockwaves under the impact of acoustic shockwaves, and it may pave the way for suitable applications in fabricating tandem heterojunction solar cells.

Keywords: Lead sulfide QDs, Shock waves, Structural stability, Morphology, Tuneable band gap, Photoluminescence.

INTRODUCTION

In the present era, rapid development has been spotted in manufacturing stable materials for device fabrication [1, 2], which is significant for withstanding efficiency in terms of performance with regard to its sensitiveness, durability, and mechanical stability under extreme environmental conditions in the leading-edge branches for aerospace, materials science, and defense applications. Because there is a tremendous possibility of being influenced by numerous factors, including gamma rays, X-rays, shockwaves, electromagnetic radiation, etc., which significantly affects the performance of optoelectronic devices. Over the last few decades, greater focus has been paid to investigating the materials under extreme conditions, which enable the suitability of materials in radar, thermal protection, space, and sensors for designing hypersonic vehicles under pressure-induced conditions [3]. Shockwaves are supersonic waves released suddenly within a limited area that possess high energy, stress, and extreme conditions of pressure and tension. It can also be referred to as the blend of both high-transient pressure and high-transient temperature that can exist for a very short duration, from a few milliseconds to microseconds.

Research groups studied solid-state materials under high-pressure and high-temperature atmospheres and found that there is the possibility of phase transitions switching from a crystalline nature to an amorphous state and vice versa, which reveals the material's behavior and structural properties under extreme conditions [4, 5]. Among the various dynamic-pressure techniques, acoustic shock waves are among the most effective methods. When acoustic shock waves are generated using shock tubes, they produce transient pressure and temperature conditions capable of interacting with materials at the atomic scale. Consequently, acoustic-shock-wave-induced phase transitions are emerging concepts [6]. Metal oxides, including CuO [7], AgO [8], ZrO_2 [9], and NiO [10], have been studied under dynamic pressure for the determination of stability for suitable applications. Some metal oxides like TiO_2 [11] and Co_3O_4 [12] undergo the phase transitions and ensure the notable changes in the structural properties with the influence of shockwaves. Furthermore, Fe_2O_3 NPs under the impact of dynamic shockwave-loaded conditions reveal the loss in degree of crystallinity [13]. Only a few sulfide materials, such as molybdenum disulfide (MoS_2), tungsten disulfide (WS_2) [14], zinc sulfide (ZnS) [15], bismuth sulfide (Bi_2S_3) [16], cadmium sulfide (CdS) [17], etc., were investigated under dynamic shockwaves for determination of reversible phase transitions and the possibility of tuning the morphology and band gap. However, each and every material has its own threshold to withstand extreme pressure or transform

---

*Address correspondence to this author at the Department of Physics, Government Arts College for Men, Krishnagiri, Tamil Nadu, India;
E-mail: vigneashwari@gmail.com

Received on 02-11-2025 Accepted on 04-12-2025 Published on 08-12-2025

E-ISSN: 000-000/25

the characteristic nature depending on the structure of the materials. For the fabrication of real-time devices, it is essential that the materials used should have the capability to withstand their properties under extreme conditions.

Lead sulfide (PbS), being a member of the IV-VI family of semiconductors, has potential applications in lasers and has a crucial role in photovoltaics and optoelectronic devices. It is a narrow band gap material, which makes PbS a perfect optoelectronic material having an exciton Bohr radius of 18 nm. The absorption edge of bulk PbS is associated with the regime of the near-infrared region (NIR) in the solar spectra, so this feature makes PbS a versatile material for photovoltaics [18]. However, long-term stability is a critical challenge for researchers, and it remains an issue because nanomaterials can undergo structural degradation and phase transformations over time. Many research groups studied PbS under various pressure conditions because the nature of PbS has a great influence under pressure. It has also been studied that at 23.0 GPa, lead sulfide gets crystallized from rock salt (B1) into a CsCl structure [19, 20]. The conclusion of many research groups confirms that the phase transformations with a reduction in grain size under high-pressure conditions lead to the enhancement of charge carrier transport behavior of PbS according to Heo *et al*. [21] and the occurrence of pressure-induced phase transitions under the influence of pressure created by diamond anvil cells (DACs) [22]. Moreover, the impact of acoustic shock waves on structural stability and tuning the optical and morphological properties of lead sulfide quantum dots (QDs) remains unrevealed. Therefore, it is essential to study the behavior of cubic-PbS QDs under acoustic pressure; henceforth, it could open the changes in properties, which could make it a promising material for shockwave-tolerant optoelectronic devices and sensors [23].

Other research groups focused on the investigation of PbS NPs under the impact of acoustic shockwaves having a Mach number of 2.2 and found them to have a stable monoclinic structure [23], whereas limited attention has been given to quantum confinement of cubic PbS. To address this research gap, the present research systematically investigates PbS QDs under the effect of acoustic shockwaves having a 1.5 Mach number, 0.59 MPa transient pressure, and a transient temperature of 520 K. The aim is to determine whether the acoustic shockwaves could induce desirable modifications in the structural, optical, and luminescent properties and morphology of PbS QDs. This study demonstrates the shockwave-induced effects of PbS QDs for ensuring their applicability in harsh environmental conditions. The experiment with lead sulfide under the impact of shockwaves was investigated using different characterization techniques.

EXPERIMENTAL SECTION

Synthesis of Lead Sulfide (PbS)

PbS was prepared by the co-precipitation route by using lead nitrate ($Pb(NO_3)_2$) and sodium sulfide (Na_2S) purchased from Sigma-Aldrich, which act as sources for Pb^{2+} and S^{2-} ions, respectively. 1M of $Pb(NO_3)_2$ was dissolved in 60 ml of deionized water (DW), which was stirred vigorously, and 1M of Na_2S was dissolved in 60 ml of DW in a separate beaker. The solutions were mixed by adding Na_2S dropwise to the solution containing the lead (Pb^{2+}) source. The stirrer rate was maintained at 500 rpm continuously for 3 hours. Ammonium hydroxide (NH_4OH) was added slowly to adjust the pH value to 8. The visible change in color of the mixture from milky white to black indicates the formation of PbS nanoparticles as shown in the following steps:

$Pb(NO_3)_2\,(aq) + Na_2S\,(aq) \rightarrow PbS\,(ppt) + 2NaNO_3\,(aq)$

The impurities were removed by continuous washing and centrifugation at 3000 rpm with ethanol and acetone for 1 hr. Finally, the obtained precipitates were dried at 80°C for 2 hrs, and the precipitates were grinded into fine powders.

Loading Shockwaves on PbS

The as-prepared samples (P1) were divided into 2 sets, namely P2 and P3. Approximately 0.5 g of each set of samples was packed in a specially designed pouch with a dimension of 10 x 10 x 1 mm^3. The specimen (sample) pouch was steadily fixed on the stainless-steel specimen holder. Using the tabletop semi-automatic Reddy tube (Yelagiri Technologies, Model: ST2024YT02), the samples were subjected to acoustic shockwaves. Figure **1** depicts the schematic representation of the shockwave tube comprising the driven, driver, and diaphragm sections, respectively. These sections possess an inner diameter of about 1.5 cm. The diaphragm section separates the other two sections, and it is fitted with an 80 GSM paper diaphragm, which is inserted into the diaphragm section manually.

The compressed driver gas (air) is fed into the driven section, and thus shockwaves are produced by rupturing the diaphragm when the critical pressure is achieved. The blasting and propagation of shockwaves in a series of 200 and 400 shock pulses having the Mach number 1.5 each, with a transient pressure of 0.59 MPa [24] and a transient temperature of 520 K

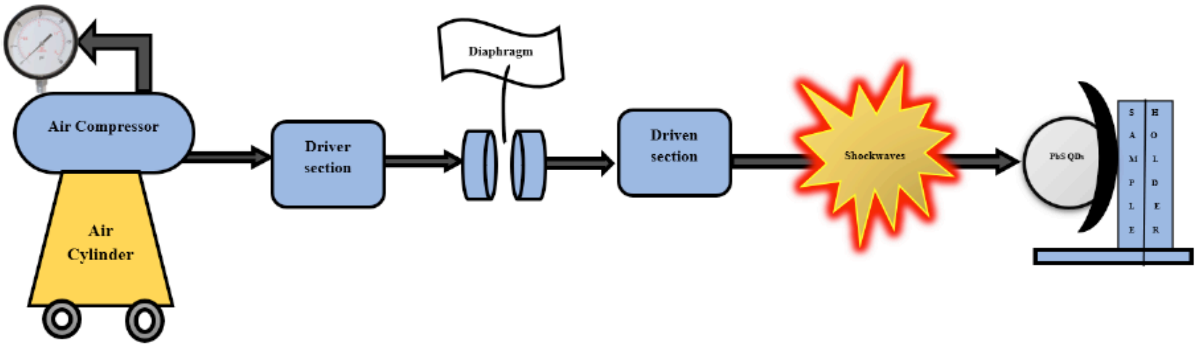

Figure 1: Schematic representation of tabletop semi-automated Reddy tube for loading shock pulses.

[25]. The strength of shock pulses was varied to 200 pulses, and the next batch of samples was for 400 shock pulses with a time interval of 5 seconds between each shock pulse. The Mach number, transient temperature and transient pressure for each shock pulse was estimated using piezoelectric PCB transducers (Model 113B26) fixed 39 cm away from the driven section, having a sensitivity of 1.465 mV kPa-1, and a linearity error of about 1%. To ensure accuracy, the calibration of transducers was performed under the identical high-pressure and high-temperature (520K) conditions [26]. The calibration procedure requires verification of the transducer's response against a standard reference having a standard error persistently below 5%. This guarantees high reliability and repeatability of transient pressure estimation, contributing an explicit baseline for investigating the effects of acoustic shock pulses on the specimen. These shockwaves propagate through the driven section approaching the lead sulfide powder mounted on the sample holder. In the present work, shock waves were loaded to PbS manually by placing the samples on the sample holder 1cm away from an open-end (the specimen is fixed outside the shock tube from the open-end of the driver tube) to ensure uniform exposure of shock waves. To access the impact of shockwaves, PbS were characterized to systematically explore the structure using powder X-ray diffraction (PXRD) analysis, high-resolution transmission electron microscopy (HRTEM), selected area energy electron diffraction (SEAD), field emission scanning electron microscopy (FESEM), energy dispersive X-ray spectrum (EDAX), UV-DRS analysis, and photoluminescence (PL) spectroscopy to observe the changes that occurred in the optical behavior before compressing and after shockwave treatment. The results were elaborately discussed.

RESULTS & DISCUSSIONS

PXRD Analysis

The crystalline structure of PbS was studied using a benchtop Bruker D2 Phaser powder X-ray diffractometer for the present study. Cu-Kα as the source having a wavelength of 1.5406Å. The PXRD pattern of unshocked (P1) PbS was compared with the standard reference pattern. The peaks appeared at 2θ values of 26.03°, 30.12°, 43.07°, 50.93°, 53.41°, 62.51°, 68.81°, 70.82°, and 78.85° of unshocked PbS (P1), and the (hkl) values were indexed at (111), (200), (220), (311), (222), (400), (331), (420), and (422) planes, respectively. The PXRD pattern of P1 was in good accordance with JCPDS card no: 78-1900; the reference pattern matches well with the obtained pattern, and all the diffraction peaks correspond to the face-centered cubic crystal structure having the space group Fm-3m (225), where F denotes the face-centered cubic lattice and m-3m stands for the point group symmetry with mirror planes and a three-fold rotation axis. It also indicates the phase purity of the cubic-PbS without traces of another phase in as-synthesized PbS. It was further determined using High Score Plus software with a search and match facility, which was confirmed by comparing it with the standard reference pattern ICDD-00-005-0592 as shown in Figure (**3**).

After that, PbS was subjected to shock pulses with magnitudes of 200 and 400 pulses. Once again, the samples underwent PXRD analysis to confirm the crystalline structure. PXRD profiles of 200 (P2) and 400 (P3) shock pulses were represented in Figure **4**, which were compared with unshocked (P1) PbS. The PXRD pattern of the samples P2 and P3 corresponds to a face-centered cubic crystal structure, which was corroborated by the standard reference pattern JCPDS card no: 78-1900. From the obtained PXRD profiles, under the influence of shockwaves, PbS showed neither the formation of new peaks nor the vanishing of peaks. In the obtained PXRD pattern of shockwave-loaded PbS of 200 and 400 shock pulses, the diffraction peak intensities decreased as compared to unshocked conditions, which shows that the periodic arrangement of atomic lattice planes of PbS is significantly affected due to the impact of shockwaves. It indicates the distortion in the lattice and formation of

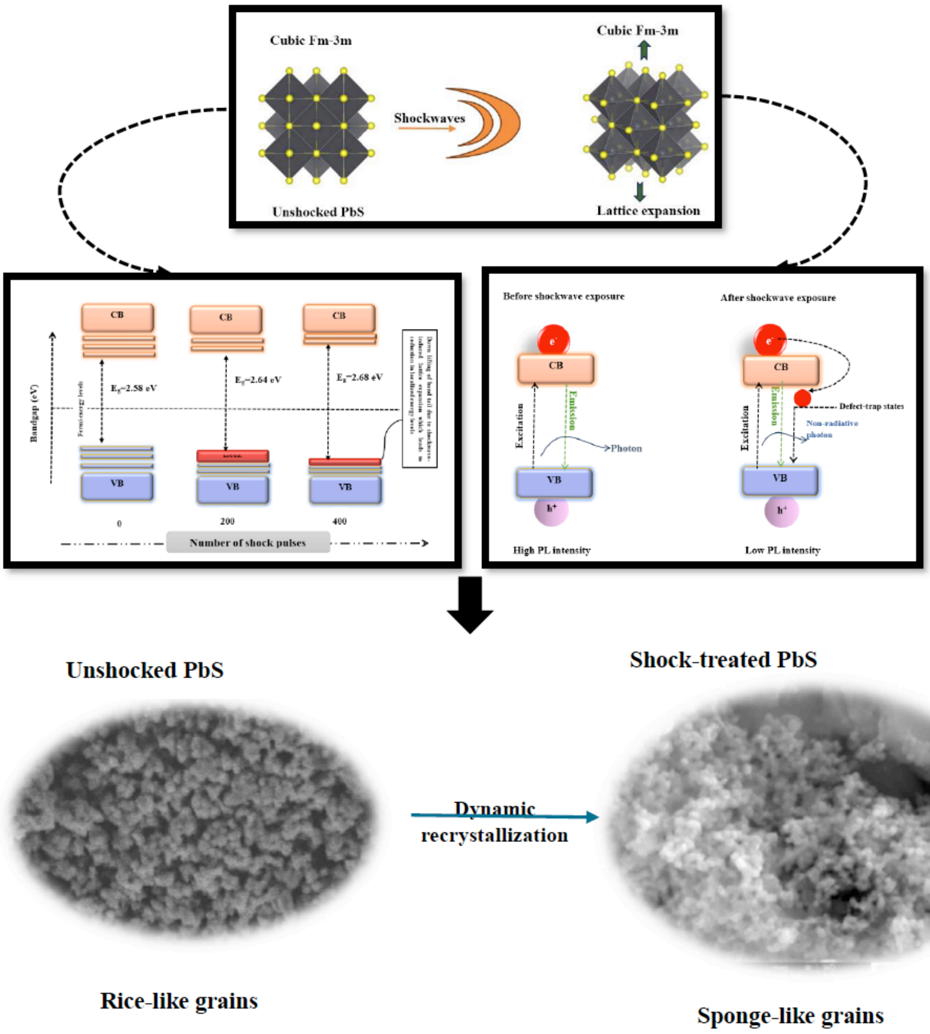

Figure 2: Schematic illustration of shock-induced modifications in PbS QDs.

defect states because of sudden variation in pressure and temperature. For a better understanding of the crystallographic phase stability of PbS, the magnified version of the (220), (311), and (222) planes, which shows the PXRD pattern from 40° to 60°, was presented in Figure (**5**). Moreover, the PXRD peaks were shifted ~0.05° towards the lower angles for the planes (220), (311), and (322) that were observed in shock-loaded conditions, indicating the emergence of residual strain within the crystal lattice [26]. Such a shifting of diffraction peaks towards lower diffraction angles indicates the sudden fusion and fission of grain boundaries under the impact of acoustic shockwaves.

The crystallite size was calculated for unshocked and shock-exposed PbS using the Debye-Scherrer relation.

$$D = k\lambda / \beta\cos\theta$$

Where D represents the crystallite size (nm), k is the Scherrer's constant (0.9), λ denotes the wavelength of X-rays (1.5406 Å), θ represents the Bragg's angle (in radians), and β is the full width at half maximum (in radians). The crystallite size of unshocked PbS is found to be 16.29 nm. The crystallite sizes of 200 & 400 shock-treated PbS are 15.51 nm and 14.27 nm, respectively. The slight variation in crystallite size might be because of mechanical forces caused by shockwaves to break down some of the larger crystallites into smaller ones having more grain boundaries. The average crystallite size has decreased as compared to the unshocked PbS (P1) because of the dynamic interplay that led to fragmentation induced by shockwaves. When shockwaves propagate through materials, it induces strain in the lattice, which leads to grain fragmentation, the enhancement in defects or lattice imperfections, and the grain boundaries. Furthermore, the calculations of lattice strain (microstrain) (ε), dislocation density (δ), and cell volume for unshocked and shockwave-loaded samples.

The average lattice strain was calculated using

$\varepsilon = \beta_{hkl} / 4\tan\theta$, where ε denotes the average lattice strain, θ corresponds to the diffraction angle, and β_{hkl} represents the full width at half maximum.

Dislocation density of PbS NPs before and after shock exposure was estimated by

$$\delta = 1/D^2$$

where D corresponds to crystallite size, which was derived from the Debye-Scherrer formula,

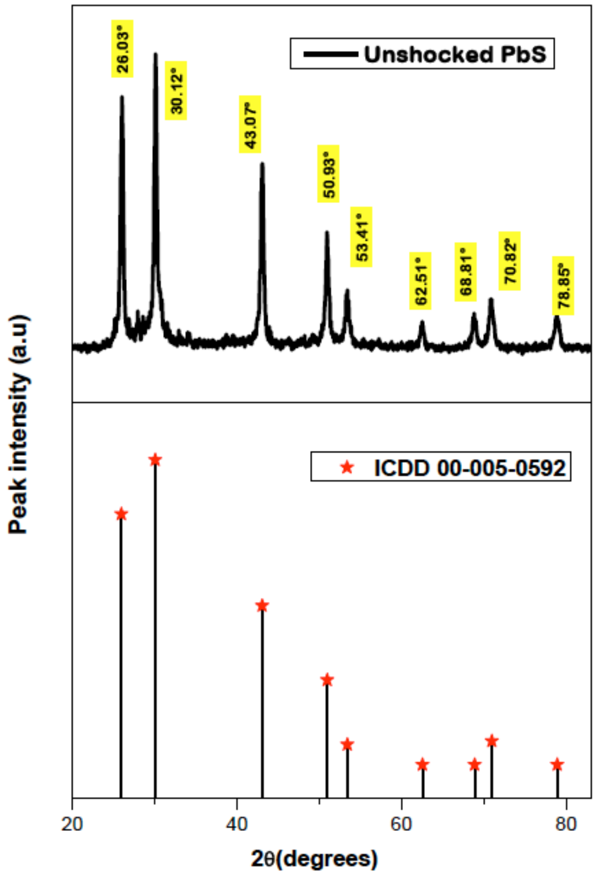

Figure 3: PXRD pattern of unshocked PbS with the ICDD reference pattern of PbS.

According to the literature, the cell volume tends to change when XRD peaks get shifted towards lower and higher angles [27], which was also obtained for PbS under the influence of acoustic shockwaves. The unit cell volume and d-spacing were evaluated using UNITCELL program software [28], in which PXRD data was used in the calculation. The lattice parameters, such as a, b, c, and unit cell volume (V), were detailed in Table **2**. This shows that under the exposure of acoustic shock pulses, the lattice parameters and unit cell volume were increased due to lattice expansion induced by shockwaves, where high pressure has driven the atoms apart, thus increasing the unit cell volume [29]. The variations in lattice parameters of PbS might be because of compressive or tensile strain [30] when subjected to acoustic shockwaves. Generally, the exposure of shock pulses has the tendency to cause rapid deformation in the crystal lattice. It can induce either lattice contraction or lattice expansion that has a direct influence on the intrinsic structural properties and response of the materials when subjected to acoustic shockwaves [31]. Such dynamics can alter the arrangement of atoms within the crystal that contributes desirable information on the degree of deformations induced by acoustic shockwaves [32]. This trend implies a dynamic balance of expansion mechanism by shock-induced defect mobility and thermal effects [33].

The changes in unit cell volume and lattice parameters contribute to defects like interstitials and defects and also slight strain in the atomic lattice, which causes slight expansion where the atoms are being displaced from their equilibrium position, thereby stretching the lattice as illustrated in Figure (**2**). During

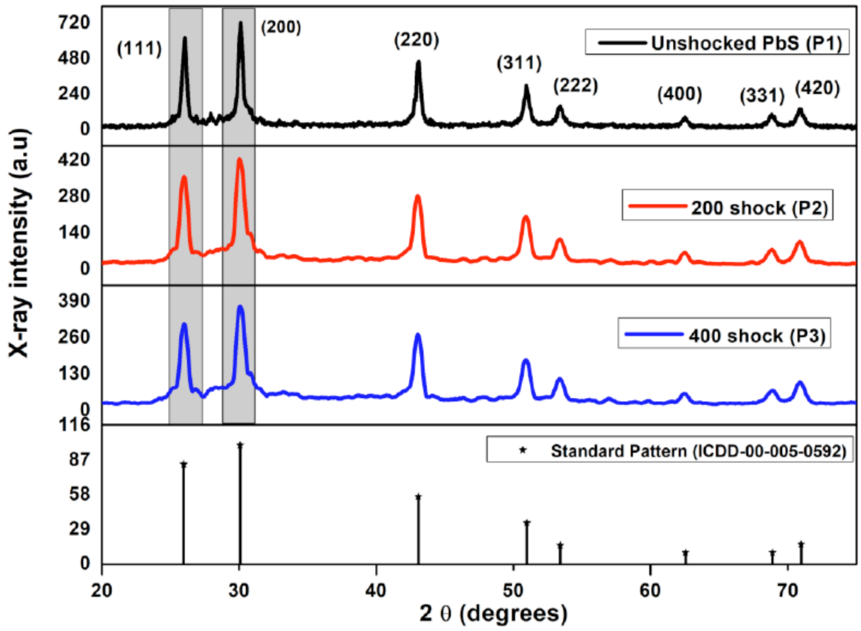

Figure 4: PXRD pattern of PbS before and after shock wave-loaded conditions.

Table 1: Crystallite siZe, FWHM, and Lattice Strain of Unshocked and Shock Wave-Loaded PbS

Sample Codes	No. of Shock Pulses	FWHM (degrees)	d-Spacing of (200) Plane (Å)	Lattice Strain (%)	Crystallite Size (nm)	Dislocation Density (lines/m²)
P1	0	0.5909	2.9215	0.001463	16.29	4.312
P2	200	0.6321	2.9323	0.001583	15.51	5.082
P3	400	0.7084	2.9405	0.001804	14.27	6.361

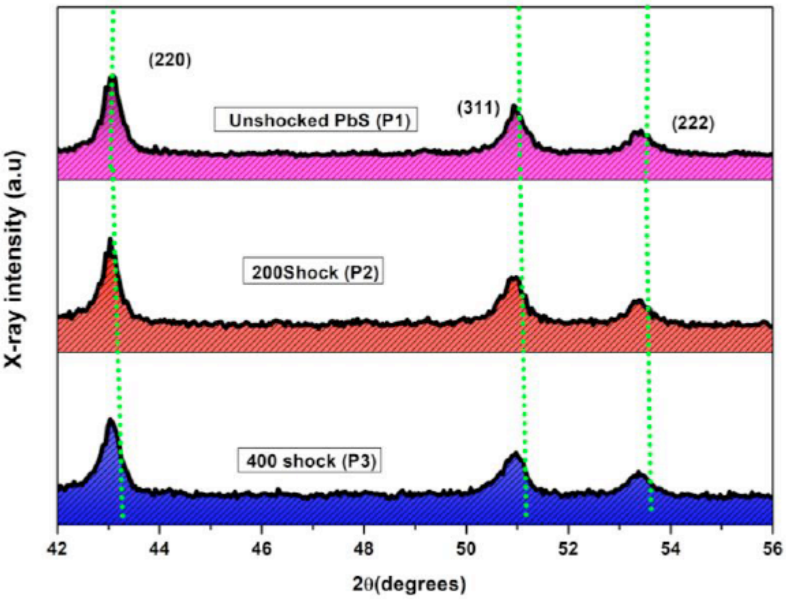

Figure 5: Magnified version of PXRD planes of (220), (311), and (222).

the shockwave exposure, a uniform tensile strain usually develops at the right angles to the direction of wave propagation [25]. The effects of shockwaves have resulted in an increase in lattice strain and FWHM values, which were reflected in the peak broadening of the PXRD pattern of 200 (P2) and 400 (P3) shock-loaded conditions, as reflected in the decrease in crystallite size. Also, an increase in lattice strain (microstrain) confirms the degradation of crystallinity and further indicates the existence of tensile strain in the lattice [25]. Figure (**7**) demonstrates the relationship between crystallite size and lattice strain is inversely proportional to the impact of shockwaves. In the present case, there is a slight increase in d-spacing at shock-treated conditions. Due to the existence of uniform strain, it led to an increment in d-spacing values, and this type of variation caused the diffraction peak positions to shift towards lower angles [33].

Rietveld refinement was performed by utilizing the “Full Prof-suite” software [34] for PbS before and after shock exposure. This gives additional confirmation of the phase stability of the PbS, which also shows the high structural stability under dynamic shockwave conditions. The well-fitted refined PXRD profiles show a perfect match and confirm the cubic structure of PbS without any phase change even after exposure to acoustic shock pulses in the increasing counts of 200 & 400 pulses. The residual factors such as R_{wp}, Rp, and $\mathcal{X}^2$ are the refinement quality indicators of weighted profile R-factor, profile residual factor, and goodness-of-fit for unshocked and shock-treated PbS, which are converged, and the values are displayed in Table (**2**). It indicates the reliability of the cubic structure before and after exposure to acoustic shock pulses. The corresponding plot was presented in Figure (**6**); the refinement parameters were acquired by the pseudo-Voigt function [34], where the peaks were fitted in the cubic (Fm-3m) space group for unshocked, 200, and 400 shockwave-loaded conditions that show the stability of the structure, and the refined plot shows the original phase preserved under high-pressure acoustic shockwaves, and the parameters were presented in Table (**2**). Therefore, the effects of pressure applied at 0.5 MPa might not be strong enough to trigger phase transformations and collapse the crystal structure. At 13.0 GPa, there is a gradual change in the diffraction peak intensities with increasing the pressure. Also, from 13.0 GPa to 29.4 GPa, there was a mixture of orthorhombic structure and CsCl-type body-centered cubic structure, as reported in [35]. However, in the present study, with the experiment of PbS with shockwaves of 0.59 MPa, there was a stable face-centered cubic structure at 200 and

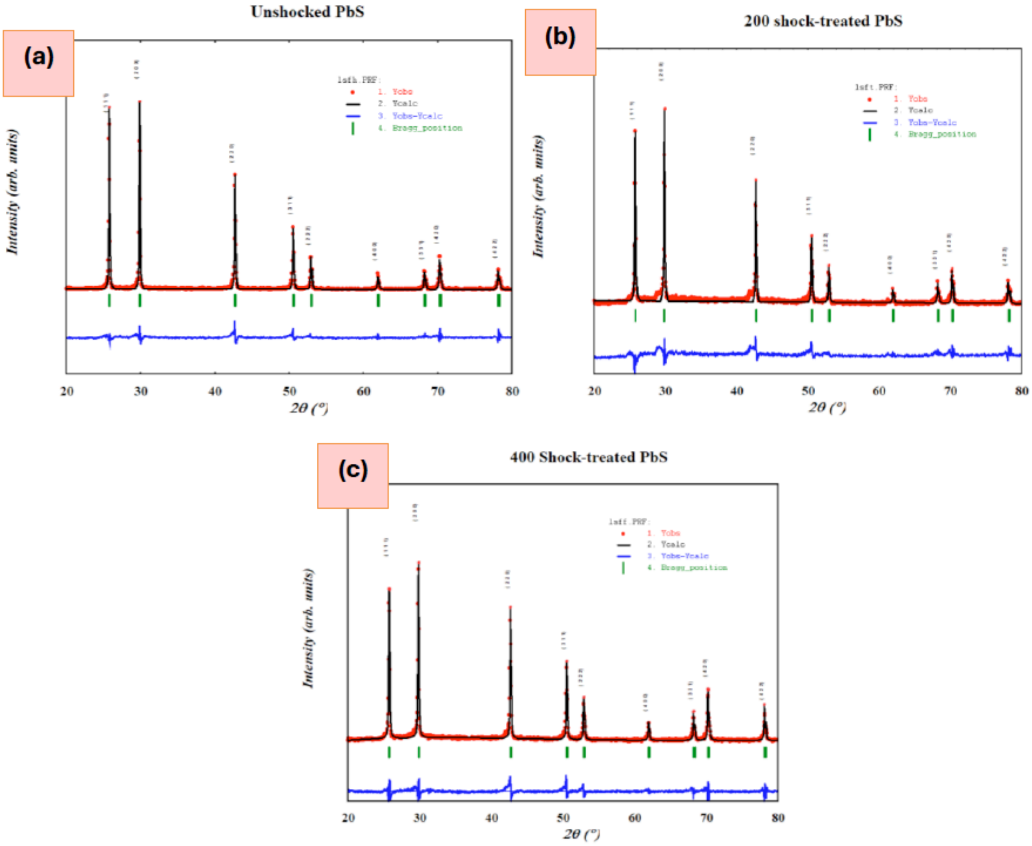

Figure 6: Rietveld Refinement Plots of (**a**) unshocked, (**b**) PbS-200, (**c**) PbS-400 shock pulses.

Table 2: Lattice Parameters of Unshocked and Shock Wave-Treated Samples

Test conditions	Unshocked PbS	200 shocks	400 shocks
Crystal structure	Cubic	Cubic	Cubic
Space group of PbS	Fm-3m	Fm-3m	Fm-3m
Lattice parameters (a=b=c)	5.936±0.002Å	5.939±0.002Å	5.941±0.002Å
α = β = γ	90°	90°	90°
Volume of unit cell (Å)³	209.24	209.57	209.73
Goodness of fit (□^{2})	1.41	1.85	1.65
R_{wp} (%)	11.90	13.52	12.36
R_p (%)	8.34	9.87	8.85

400 shockwave-treated conditions. Hence, from the investigations, it is clear that PbS maintains structural integrity and did not undergo any crystallographic phase transformations. Considering the observations on shock resistance, PbS holds the crystallographic phase stability better than the lead nitrate crystals [5] under dynamic shockwaves, so PbS NPs can be a good option for utilization in high-performance devices.

Transmission Electron Microscopy (TEM) Analysis

Transmission electron microscopy (TEM) analysis was performed using JEOL JEM-2100 with an operating voltage of 200kV. For the specimen preparation, PbS was dispersed in ethanol and sonicated to achieve a homogeneous dispersion. A aliquot part of the dispersoid was seized using a hypodermic needle and sprayed on the top of a carbon-coated copper grid. The grid was carefully dried and loaded into the TEM vacuum chamber and the analysis was performed. In Figure (**8**), the TEM image of unshocked and shock-treated PbS exhibits a closely packed ultra-small particles embedded matrix and the corresponding electron diffraction patterns were presented. TEM micrographs shows that the particles are aggregated and are irregularly shaped where the estimation of particle size was quite difficult. Since, the unshocked and shock-exposed PbS exhibit the average crystallite size within the range of excitonic Bohr radii (r_B=18nm), HRTEM analysis could confirm the actual existence of ultra-fine sized particles. For clear understanding of the microstructure of PbS before and after loading shockwaves; the HRTEM micrographs are presented in Figure (**8**) The lattice fringe spacing (d-spacing) were 2.93Å which corresponds to d_{200} plane [36] of cubic PbS lattice (as presented in the inset of Figure (**9**)). The enlarged HRTEM images shows the shock-treated PbS QDs are highly crystalline indexed to cubic rock-salt structure, where the lattice fringe spacing for 200 shock-treated PbS 2.94Å and 2.97Å corresponding to the interplanar spacing of d_{200} crystal plane [37, 38]. The average particle size was calculated from the HRTEM images using ImageJ software and the corresponding histogram profiles were presented. It clearly shows that the size of particles is within the range of 18 to 20nm for unshocked PbS, 14 to 17nm for 200 shock pulses, and 10 to 15nm for 400 shocked PbS. Under the exposure of 200 and 400 shock pulse, the mean particle size of QDs were reduced as seen in Fig Figure (**10**). The average crystallite size calculated using the Scherrer equation in PXRD analysis corroborates with the particle size that calculated from HRTEM images. As per the literature, the particle and crystallite sizes are interrelated to each other [25]. These variations were attributed to shockwave exposure, which caused dynamic recrystallization, thereby altering the particle size of shock-treated samples. The fusion of grain boundaries was also noticed under the impact of shockwaves, which was also reported in our previous publication [17].

As shown in Figure (**7**), the ring-type selected area electron diffraction (SAED) pattern of unshocked and

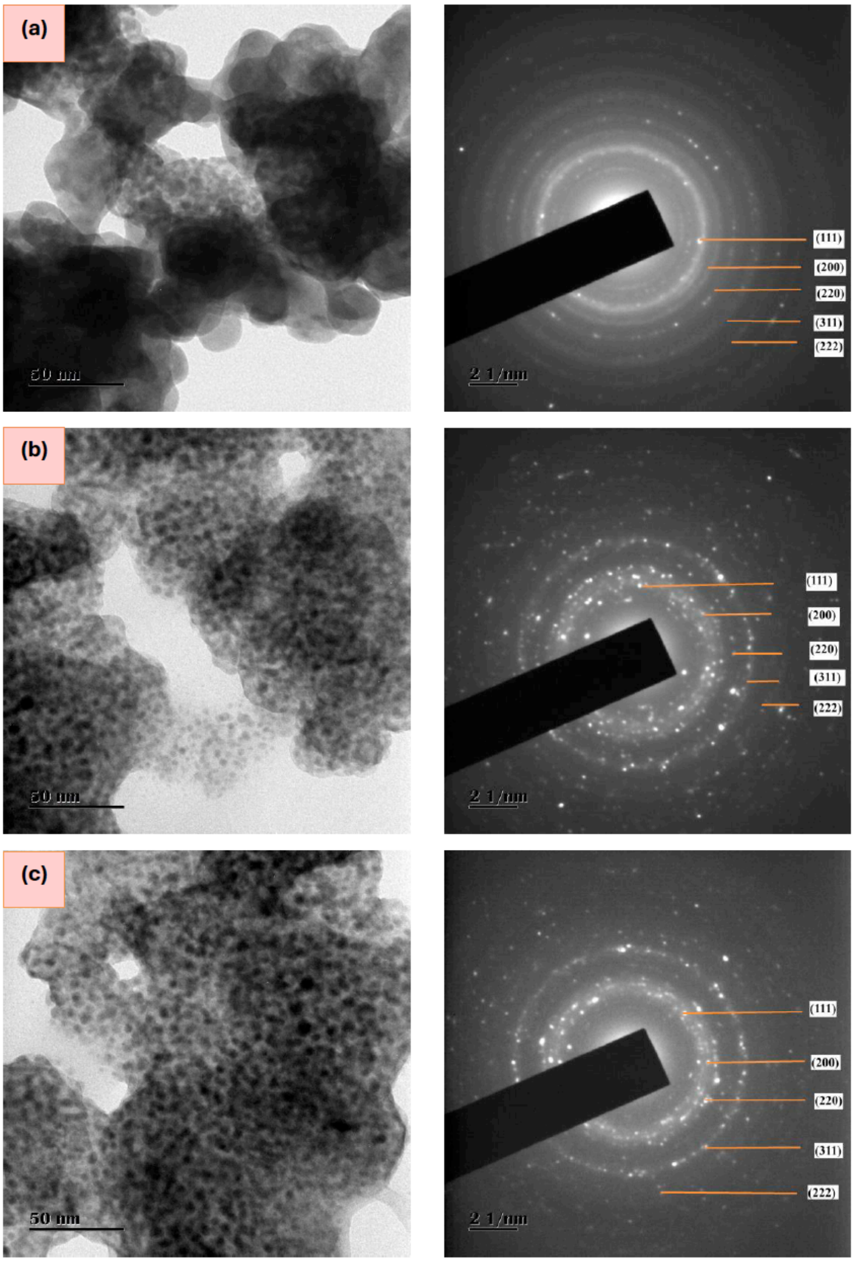

Figure 8: TEM micrograph and corresponding SAED patterns of (**a**) unshocked, (**b**) 200, and (**c**) 300 shock-treated PbS.

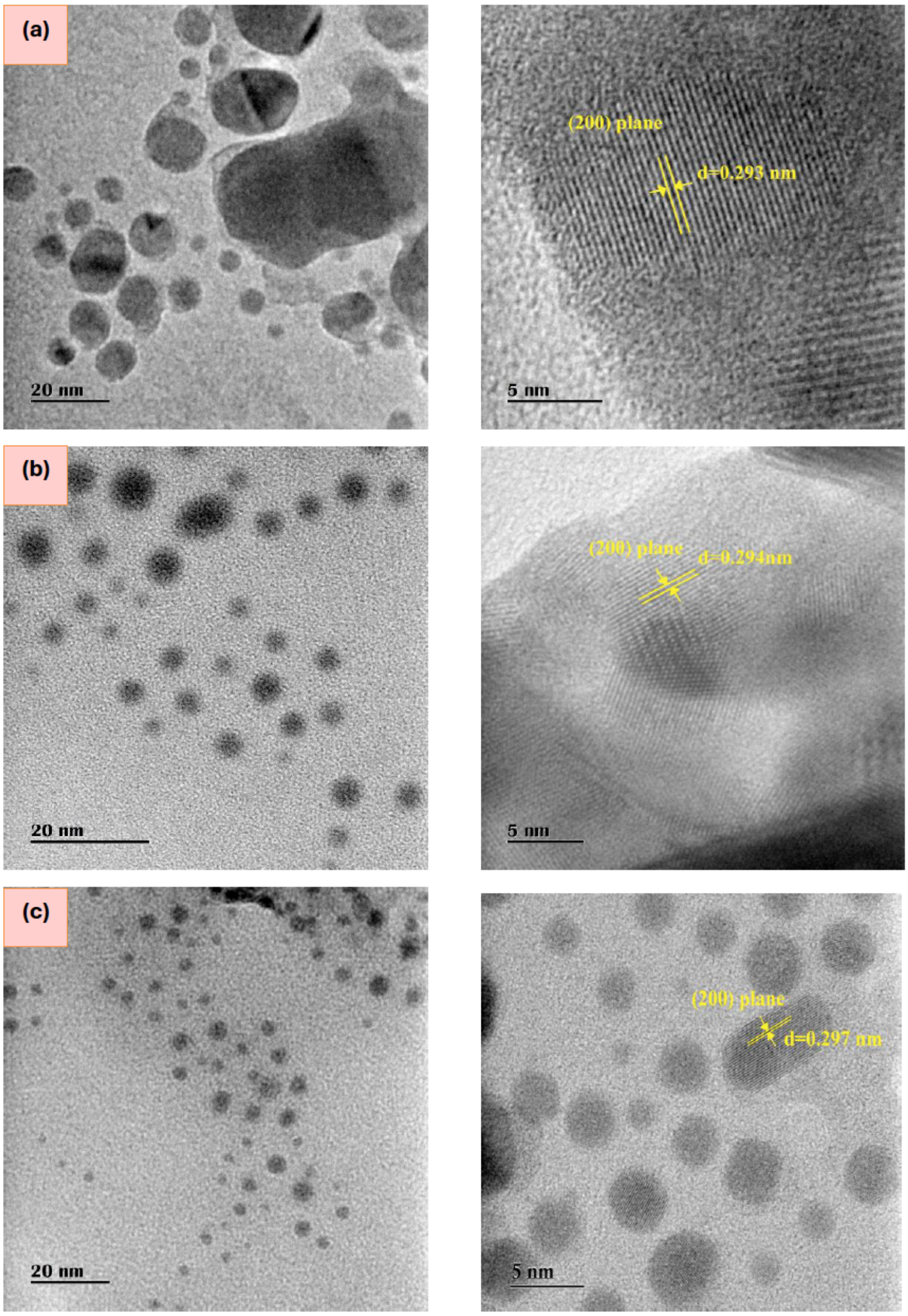

Figure 9: HRTEM micrographs of (**a**) unshocked, (**b**) 200 shock, and (**c**) 300 shock-treated PbS.

200 and 400 shock-treated PbS is indexed to families of planes (111), (200), (220), (222), and (400) of cubic structure, which is in good accordance with PXRD results and well matches with JCPDS card no. 78-1900. The interplanar distance of the (200) plane calculated from diffraction rings was well-matched with that calculated from PXRD analysis and the HRTEM image for unshocked and shock-treated conditions. It is evident that from SAED patterns, the crystallographic phase of PbS QDs belonging to the cubic crystal structure is retained even under 200 and 400 shock-loaded conditions. Also, the obtained SAED pattern of unshocked PbS shows the formation of ultra-fine crystalline QDs revealed by the bright diffraction spots oriented randomly, indicating the nanoscopic particles in different directions. At shock-treated conditions, the appearance of diminished diffraction spots could be seen denoting the reduction in degree of crystallinity as corroborated with PXRD results, where the X-ray peak intensity reduced at shock-loaded conditions, but there were no signs of phase transformation under the influence of acoustic shockwaves. This gives direct evidence that PbS QDs have high shockwave resistance and have a stable cubic structure when exposed to acoustic shock pulses.

Morphology of PbS QDs

For morphological characterization, a scanning electron microscope (SEM) of model Carl Zeiss

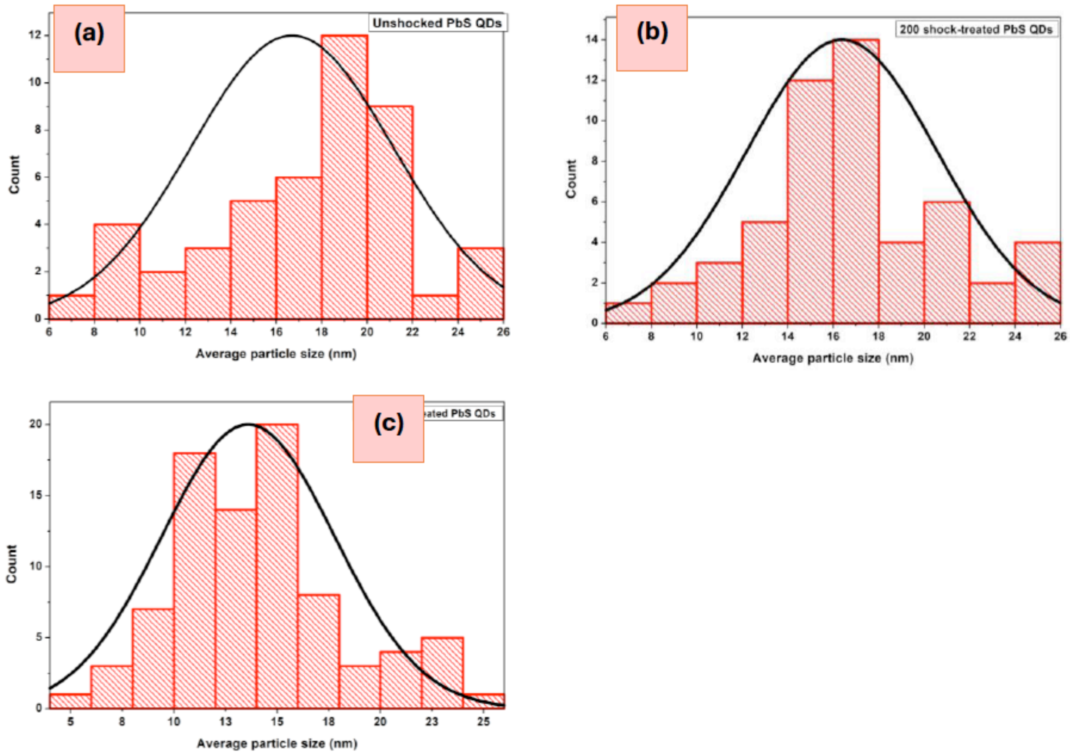

Figure 10: Average particle size distribution of (**a**) unshocked, (**b**) 200 shock, and (**c**) 400 shock-treated PbS QDs.

EVO-18 with a resolution of 3 nm for analyzing morphology at lower magnification and a field emission scanning electron microscope (FESEM) of model Apreo 2s HiVac were used for this experiment to characterize the morphology of shock-treated PbS at higher magnification with a resolution of 4 nm. The specimen was mounted on a double-sided conductive adhesive tape, carefully secured on a stub holder. The SEM equipment operates with an accelerating voltage ranging from 0.5 to 20 kV and has a magnification ranging between 1x and 100,000x. FESEM operates with an accelerating voltage range from 200 V to 30 kV and a magnification from 20x to 1,000,000x. Energy Dispersive X-ray Analysis (EDAX) was used to characterize the unshocked PbS NPs for examining the elemental composition of the specimen. A ZEISS scanning electron microscope coupled with the EDAX system was used to map the spectrum. Figure (**11**) shows the EDAX spectrum of unshocked PbS Both imaging and analysis were carried out at several locations of the specimen and unshocked sample is found to show the major presence of Pb and S in the as-prepared unshocked sample. Other signals noticed would have originated from the grid during data acquisition. As shown in the Figure (**12**, **13**) which represents the SEM image unshocked PbS and FESEM images of 200, and 400 shock-loaded samples. SEM image of unshocked PbS QDs shows that the particles are clumped together. At 200 shocks, it can be seen that the particles begin of break apart which led to reduction in overall particle size indicating the shockwaves caused disruption to interparticle connections thereby resulting initial fragmentation. At 400 shock pulses, particles show the continuous reduction in particle size as witnessed from HRTEM analysis, that might be because of the combined effects of fragmentation and compaction at higher shock levels which broke down the larger particles by compressing the particle's surface.

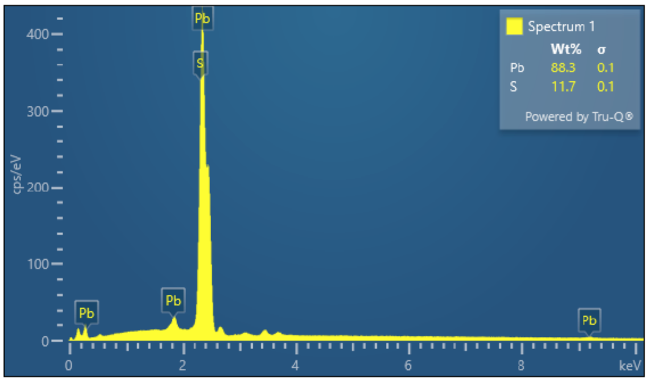

Figure 11: EDAX spectrum of PbS.

This analysis shows that the shockwave treatment of PbS is accompanied by a reduction in agglomeration. Also, this shows that at shock-loaded conditions, the particles have broken into ultra-fine particles that caused a reduction in particle size distribution. It is evident from the SEM image of shock-untreated PbS that there are very minute-sized rice-like grains embedded by numerous crystallites, as reported in [39]. Interestingly, at shock-exposed conditions, sponge-like grains were observed. It also reveals that the rice-like grains have transformed into sponge-like structures due to dynamic recrystallization induced by acoustic shockwaves because it has a significant influence on the morphology of the test material because of its low thermal transport values. Consequently, the substantial reduction in particle size at shock-exposed conditions is because of the lower thermal conductivity of PbS (2.2 W/m K) [40], which limits the heat dissipation and leads to the accumulation of thermal energy, thereby promoting dynamic recrystallization. By the sudden impact of the acoustic shock pulse, PbS QDs experience a superheating effect within milliseconds. Due to the poor thermal conductivity of PbS, it couldn't dissipate the shock-induced thermal energy immediately. This process could be understood as dynamic recrystallization, which is a combined effect of localized superheating followed by rapid cooling induced by shockwaves [41]. Upon the exposure of shock pulses, rapid cooling leads to the supercooling effect, where there is inadequate time for larger crystals to grow, leading to the formation of smaller grains. Despite the observed changes, the interplay of pressure and temperature did not modify the underlying cubic crystal structure. According to the literature, it is usual that, for face-centered cubic structure, PbS has thermodynamical stability [42]. The findings underscore the role of thermal effects induced by acoustic shockwaves, which led to variations in morphological aspects, and it also emphasizes the tuneable morphology through shockwave exposure by maintaining the structural stability of PbS. So, this may open new avenues for the betterment and designing of efficient real-time devices.

Ultraviolet-visible Diffuse Reflectance (UV-DRS) Spectroscopy

The understanding of the optical properties of unshocked and shock-influenced PbS was analyzed using a Jasco-UV-Vis-NIR (V-770, Serial No. A012061801) spectrophotometer in the range of 300 and 800 nm. Figure (**14**) represents the UV-DRS spectra of the samples. The absorption edge of unshocked PbS was found to be at 498 nm. Still, when subjecting the sample to 200 and 400 shock pulses, the absorption cutoff region was shifted to 495 nm and 492 nm, respectively. The impact of shockwaves onto the PbS QDs experiences extreme pressure and temperature, leading to fluctuation in the electronic band structure, which changes the absorption edge.

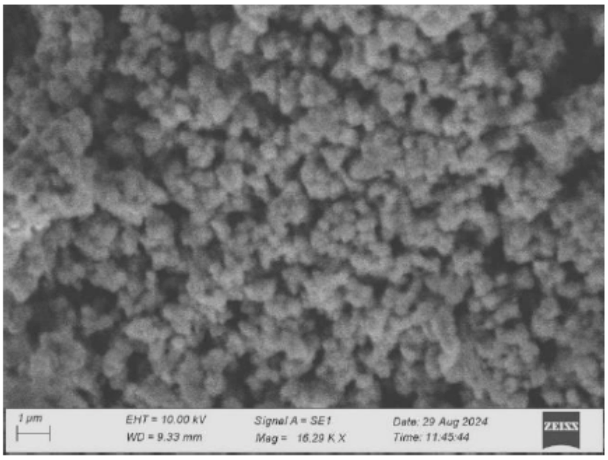

Figure 12: SEM image of unshocked PbS NPs.

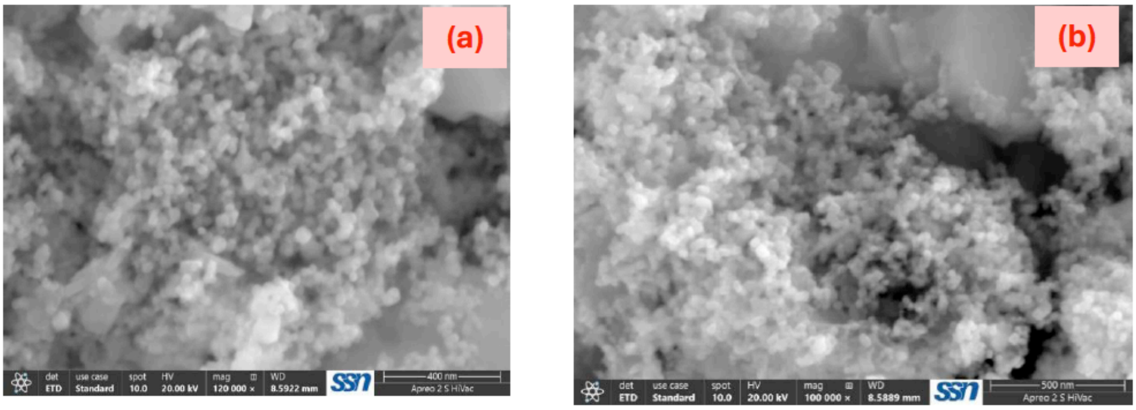

Figure 13: FESEM images of (**a**) 200 and (**b**) 400 shockwave-loaded samples.

The subsequent electronic band structure changes were caused by shockwaves, which made the wavelengths shift towards shorter ones.

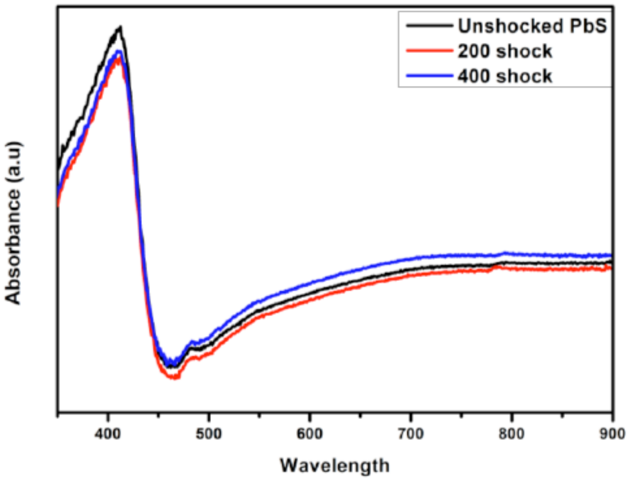

Figure 14: UV-Vis DRS spectra of unshocked and shock-loaded PbS.

The significant enhancement in unit cell volume is supported by a shift of absorption edges towards a higher wavelength at shock-treated conditions. The absorption wavelength (λ_{max}) gets shifted to larger ones as the particle size decreases because the bandgap increases at nano dimensions [43]. Furthermore, it is essential to evaluate the optical band gap energy (E_g), illustrating the difference between the valence band and conduction band of PbS at shock-loaded conditions because the test sample is one of the potential materials for optoelectronic applications. Tauc's plot relation was used to measure the band gap energy of unshocked and shock-loaded PbS QDs. By extrapolation of the linear region of the Tauc plot towards the x-axis by the following relation: $\alpha h\nu = A (h\nu - Eg)^n$. Figure (**15**) depicts the graph plotted between $(\alpha h\nu)^2$ versus hν, and the obtained plots were presented. The direct band gap energy has been evaluated, and there is a noticeable change with the Eg values of 2.58 eV, 2.64 eV, and 2.68 eV for unshocked, 200, and 400 shocked samples, respectively. According to the literature, PbS NPs have been reported to have a possible bandgap from 0.41 eV to 5.2 eV by varying their size and shape compared to bulk PbS [44, 45]. The quantum confinement has occurred due to overlapping of energy levels, causing the blue-shift in the absorption spectrum [46] by slightly increasing the bandgap energy. This corroborates that the lattice expansion has occurred, which led to the gap between the valence band and the conduction band increasing considerably under the influence of shockwaves.

For instance, defects such as interstitials, vacancies, stacking fault, grain boundaries could act as trapping centres thereby affecting the optical absorption. According to effective Brus' model, the band gap energy is inversely proportional to the particle size [47], as displayed in Figure (**16 a**). The variation in the bandgap energies might be due to the structural disorders or defects induced by the impact of shockwaves leading to the Fermi energy level and thereby generating localized states within the bandgap energy further leading to alteration in electronic properties of the material and thus causing increase in

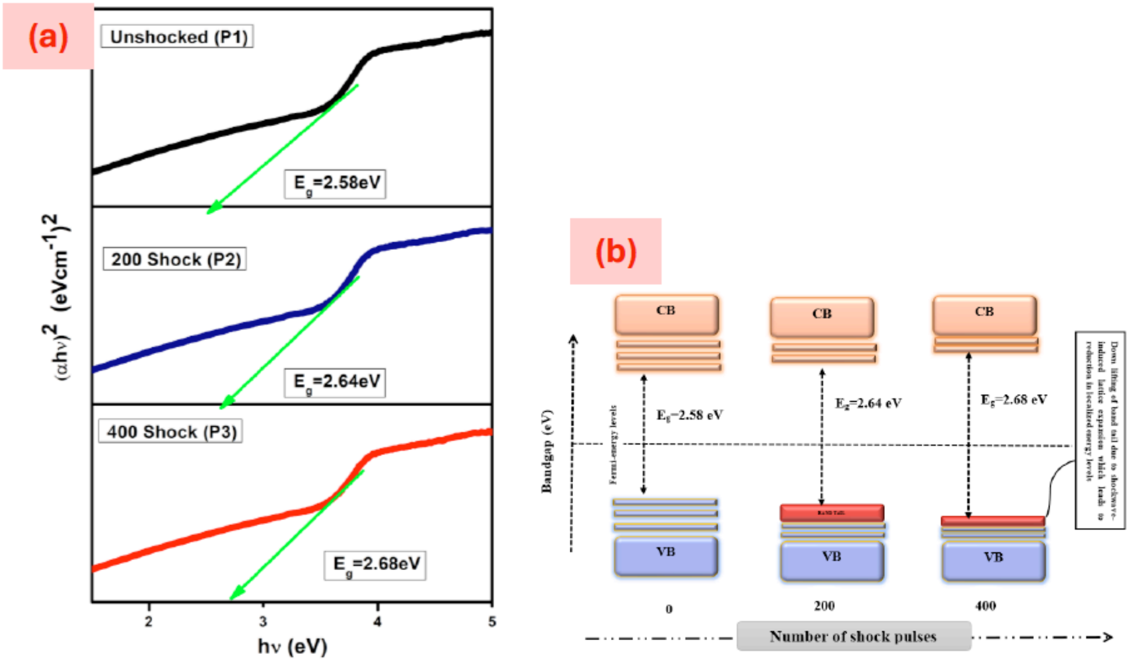

Figure 15: (**a**) Bandgap energy plot of unshocked and shocked PbS NPs, (**b**) Energy-level diagram of unshocked and shock-treated PbS QDs.

bandgap [48] as shown in Figure (**15 b**), which energy level diagram representing the alignment of bandgap under the exposure of shockwaves. The unshocked PbS shows broader absorption because of wider distribution of localized energy states near the valence and conduction bands, referred as Urbach band (Band tail). Under shock-exposure, localized energy states are decreased because, acoustic shockwaves have annealed out valence and conduction bands and moved farther resulting in a wider band gap. Figure (**16**) shows the variation plot of crystallite size versus bandgap and unit cell volume versus bandgap as a function of number of shock pulses. Hence, this study demonstrates that extreme pressure caused by shockwaves has the capability to tune the bandgap by the formation of defects and strain in the lattice as evidenced in XRD analysis. And so, PbS NPs can be suggested as candidates for applications like photodetectors, sensors, optoelectronics, and photovoltaic cells [49] at extreme conditions of pressure and temperature.

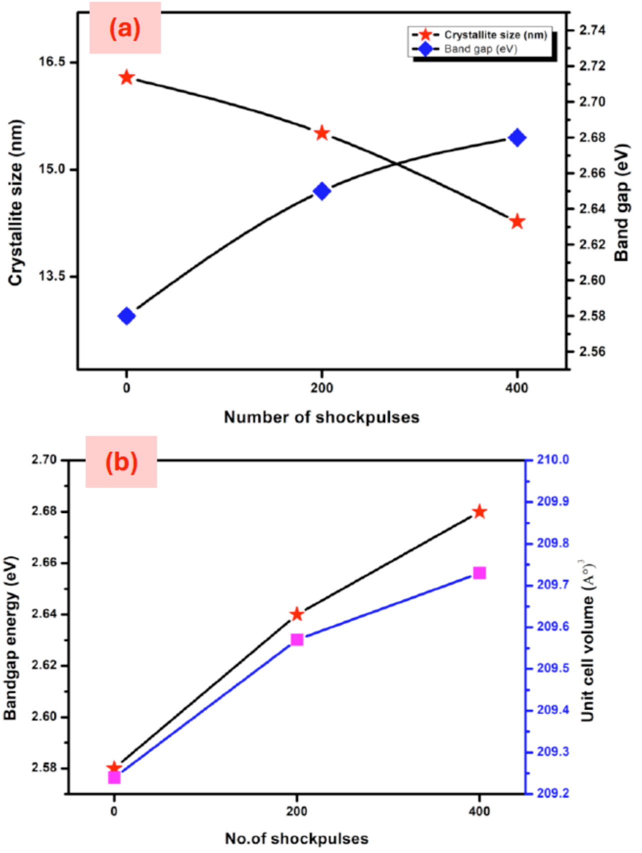

Figure 16: Variation plot of crystallite size versus bandgap of unshocked and shock-exposed PbS QDs.

Photoluminescence Spectroscopy (PL) Analysis

Photoluminescence (PL) spectra of unshocked and shock loaded-PbS QDs were recorded by using a fluorescence spectrophotometer, where the specimen absorbs light and emits the photons at a particular wavelength depending on the materials which give the information about the emission band for understanding the optical properties using Perkin Elmer Model -LS45 within the range 500 to 900nm at room temperature with an excitation wavelength of 500nm Figure (**17 a**) demonstrates the PL spectra of PbS before and after loading the shock pulses. The obtained spectra reveal the variations in PL intensities. The shock-unexposed and shock-exposed PbS exhibited a strong emission peak centred at 792nm which was well matched with the previous reports [50]. It can be clearly seen that, at unshocked conditions, the PL intensity was moderately high due to reduced defect density. The subsequent drop in the in the PL intensity provides information about the shock response of PbS QDs are caused by increased molecular interactions because of sudden changes in pressure and temperature within the crystal structure. The temperature and pressure variation can change the recombination pathways leading the PL intensity to either increase or decrease depending on the variations that occur in the electronic band structure. Also, the PL intensity is often associated with the crystallinity of the materials. Smaller crystallites generally have higher values of strain and defect densities making them less favourable for radiative recombination process. Therefore, the relationship between crystallite size and PL intensity are twofold (*i.e.*)., For larger crystallites, the lattice defects and dislocation density reduce thus leading to lower defect-related scattering and simple electron-hole pair recombination routes. At shock-loaded conditions, the decrease in PL intensity indicates the appearance of non-radiative recombination centres caused by high energetic shockwaves due to the introduction of defect states that non-radiatively trap the energy [25].

Figure (**17 b**) displays the CIE chromaticity diagram of PbS, which is used to study the color perception before and after exposure to shock waves using CIE coordinates calculator software [51]. As per CIE, the color characteristics of any light source or materials could be described in terms of a two-dimensional x-y plot, which represents the amount of red and green, blue vertex regions and emission color coordinates of the luminescent materials respectively. The CIE coordinates are obtained at x = 0.554 and y = 0.448, which are denoted by black-coloured symbols. This reveals that the obtained emission spectra of unshocked and shock-treated PbS emit color near to orange-red region which is consistent with the previous reports [52]. The x-values consistently exceeded the y-values, indicating the prevalence of near-infrared emission, which is characteristic of quantum-confined PbS. The photoluminescence lifetime measurements were calculated using single exponential fitting with help of Sci-sim lifetime calculator and found to be

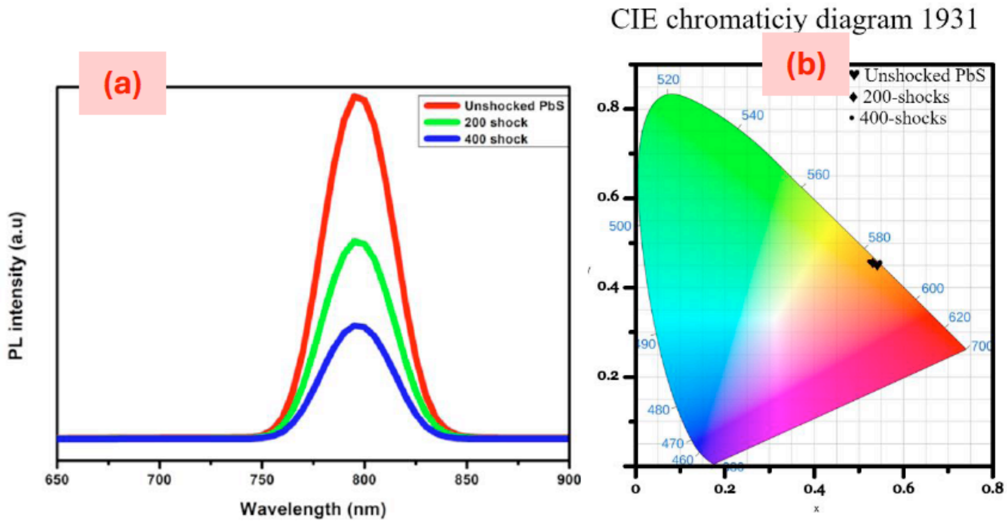

Figure 17: Photoluminescence spectra (PL) of unshocked and shock-loaded PbS NPs, (**b**) Chromaticity diagram of unshocked and shock-treated PbS QDs,

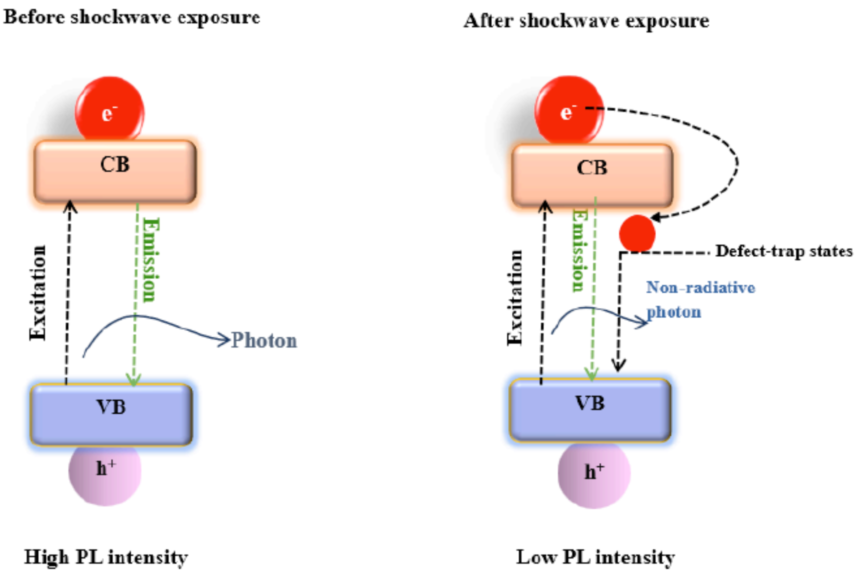

Figure 18: Mechanism of recombination pathways of unshocked and shock-treated PbS QDs.

28.5ps, 33.6ps, 37.6ps for unshocked, 200 and 400 shock-treated PbS which was well-matched with the previous reports [53]. Radiative and non-radiative recombination pathways plays are crucial role in governing the carrier dynamics of PbS before and after exposure of shock waves.

Before exposure to shockwaves, a high PL intensity is observed where more energy is released as light during the electron-hole pair recombination, thereby enhancing the probability of radiative recombination as electrons return to the valence band (VB). In addition, reduced lattice defects such as lattice strain often lead to more efficient charge carrier recombination in unshocked conditions. In shock-treated PbS, the non-radiative recombination is predominantly governed by defect states and surface traps, which introduce the rapid decay channels, thereby significantly shortening the PL lifetime. Also, the decrease in PL intensity confirms the non-radiative recombination where the energy dissipates through phenomena such as defect states or phonon interactions instead of emission of photons and lattice vibrations that convert energy into heat. Defects produce trap states in the band gap, thereby allowing the excitons to recombine without emission of photons as shown in Figure (**18**). The effect of size is ascribed to the confinement of charge carriers, which are related to short PL lifetimes under the exposure of acoustic shockwaves. The shorter lifetime attributed to quenching of PL intensity under shockwaves was because of high conductivity that resulted from efficient carrier charge separation and lower recombination [54].

The correlation between luminescent properties and lattice defects, microstrain was reported in [55] as a function of thermal treatment which was further caused by dislocations and lattice distortions that influence bandgap which cause changes in absorption and luminescence properties by modifying the energy levels [56, 57]. A reduced PL intensity of shock-treated samples suggests the reduced radiative recombination due to increased charge carrier separation which is a crucial factor for enhancing the solar cell efficiency. These findings reveal that PL intensity is not only related defects but it is also influenced by electronic factors induced by the shock pulses. These insights of PbS QDs under the extreme conditions of temperature and pressure, demonstrate its suitability in the device-based applications and solar cell technology. These properties suggest that PbS QDs could be engineered to maintain efficiency under the shockwaves which can be used for fabrication of shockwave-tolerant solar cells for enhancing performance by improving charge carrier dynamics.

CONCLUSION

In summary, the present research has been focused on the experimental investigation of the structural, morphology and optical properties of unshocked and post-shock wave loaded PbS QDs. The powder XRD analysis distinctly shows that there were no crystallographic changes occurring at the shockwave-treated sample of 200 and 400 counts. PbS QDs have high phase stability, where the cubic phase was preserved when increasing the shock pulses of 0.59 MPa transient pressure, and it was further verified using Rietveld refinement of PXRD data and HRTEM/SAED analysis. FESEM images show a consistent morphology transformation from rice-like grains into sponge-like grains without modifying the underlying cubic crystal structure PbS QDs. The profiles of the UV-Vis-DRS study and photoluminescence analysis provide the supporting shreds of evidence to justify the slight variation in electronic structures and thus widening the bandgap from 2.58 eV to 2.68 eV under the impact of acoustic shockwaves. These findings emphasize ongoing efforts for advanced materials with high performance and durability under extreme conditions of temperature and pressure, leading to innovation in solar energy harvesting technologies. Overall, PbS is emerging as a potential candidate for applications subjected to acoustic shockwaves in terms of stability and durability for optoelectronics and tandem heterojunction solar cell technologies. Such materials are crucial for maintaining the integrity and improving the performance of the devices when subjected to intense pressures, high-impact forces. The significance of shockwave-tolerant materials is the extended life span, thereby assuring safety and systematic operation of materials under extreme conditions.

DISCLOSURE STATEMENT

No potential conflict of interest was reported by the author(s).

AUTHOR CONTRIBUTIONS

Yoga Indra Eniya. R - Conceptualization & Writing original draft preparation: Vijaykumar. K-Formal analysis, F. Irine Maria Bincy-Data processing, Vigneashwari. B-Supervision

COMPETING INTERESTS

The authors have no relevant financial or non-financial interests to disclose.

DATA AVAILABILITY STATEMENT

The data in this manuscript can be obtained from the corresponding author.

REFERENCES

[1] Sivakumar, A., Ramya, S., Dhas, S. S. J., Almansour, A. I., Kumar, R. S., Arumugam, N.,& Dhas, S. M. B. Assessment of crystallographic and electronic phase stability of shock wave loaded cubic cerium oxide nanoparticles, Ceramics International, (2022), 48(2), 1963-1968. https://doi.org/10.1016/j.ceramint.2021.09.281

[2] Koteeswara Reddy, N., Jayaram, V., Arunan, E., Kwon, Y.B., Moon, W.J., Reddy, K.P.J.: Investigations on high enthalpy shock wave exposed graphitic carbon nano particles. Diam. Relat. Mater. 2013, 35, 53-57, https://doi.org/10.1016/j.diamond.2013.03.005

[3] P. Onufrijevs, A. Medvids, E. Daukšta, H. Mimura, M. Andrulevicius, N. Berezovska, I. Dmitruk, L. Grase, G. Mežinskis, The effect of UV Nd:YAG laser radiation on the optical and electrical properties of hydrothermal ZnO crystal, Optics and Laser Technology, 2016, Vol.86, 21.-25. https://doi.org/10.1016/j.optlastec.2016.06.009

[4] Ulvestad A, Welland MJ, Cha W, Liu Y, Kim JW, Harder R, Maxey E, Clark JN, Highland MJ, You H, Zapol P, Hruszkewycz SO, Stephenson GB. Three-dimensional imaging of dislocation dynamics during the hydriding phase transformation. Nature. Mater. 2017, 16, 565-571. https://doi.org/10.1038/nmat4842

[5] A. Sivakumar, P. Eniya, S. Sahaya Jude Dhas, Raju Suresh Kumar, Abdulrahman I. Almansour, Kundan Sivashanmugan, J. Kalyana Sundar and S. A. Martin Britto Dhas, Shock wave induced phase transition from crystalline to the amorphous state of lead nitrate crystals, Cryst. Eng. Comm, 2022, 24, 52. https://doi.org/10.1039/D1CE01366A

[6] A. Sivakumar, S. Sahaya Jude Dhas and S. A. Martin Britto Dhas, Assessment of crystallographic and magnetic phase stabilities on MnFe2O4 nano crystalline materials at shocked conditions, Solid.State.Sci., 2020, 107, 106340-106345. https://doi.org/10.1016/j.solidstatesciences.2020.106340

[7] A. Rita, A. Sivakumar and S. A. Martin Britto Dhas, Influence of shock waves on structural and morphological properties of copper oxide NPs for aerospace applications, J. Nanostruct. Chem., 2019, 9, 225-230. https://doi.org/10.1007/s40097-019-00313-0

[8] A. Rita, A. Sivakumar, S. Sahaya Jude Dhas and S. A. Martin Britto Dhas, Structural, optical and magnetic properties of silver oxide (AgO) nanoparticles at shocked conditions, J. Nanostruct. Chem., 2020, 10, 309-316. https://doi.org/10.1007/s40097-020-00351-z

[9] V. Jayaram and K. P. J. Reddy, Experimental study of the effect of strong shock heated test gases with cubic zirconia, Adv. Mater. Lett., 2016, 7, 100-150. https://doi.org/10.5185/amlett.2017.6379

[10] A. Rita, A. Sivakumar and S. A. Martin Britto Dhas, Investigation of Structural and Magnetic Phase Behaviour of Nickel Oxide Nanoparticles under Shock Wave Recovery Experiment, J. Supercond. Novel Magn., 2020, 1, 1-5.

[11] S. Kalaiarasi, A. Sivakumar, S. A. Martin Britto Dhas and M. Jose, Shock wave induced anatase to rutile TiO_2 phase transition using pressure driven shock tube,Mater. Lett., 2018, 219, 72-75. https://doi.org/10.1016/j.matlet.2018.02.064

[12] A. Sivakumar, S. Soundarya, S. Sahaya Jude Dhas, K. Kamala Bharathi and S. A. Martin Britto Dhas, Shock Wave Driven Solid State Phase Transformation of Co_3O_4 to CoO Nanoparticles, J. Phys. Chem. C, 2020, 124, 10755-10763. https://doi.org/10.1021/acs.jpcc.0c02146

[13] A Rita, A Sivakumar, M Jose and S A Martin Britto Dhas, Shock wave recovery studies on structural and magnetic properties of α—Fe_2O_3 NPs, Mater. Res. Express 2019,6, 095035. https://doi.org/10.1016/j.cplett.2013.07.044

[14] K. Vasu, H.S.S.R. Matte, Sharmila N. Shirodkar, V. Jayaram, K.P.J. Reddy, Umesh V. Waghmare, C.N.R. Rao, Effect of high-temperature shock-wave compression on few-layer MoS_2, WS_2 and $MoSe_2$, Chem. Phys. Lett. 582 (2013) 105-109.

[15] Sivakumar Aswathappa, Lidong Dai, Sahaya Jude Dhas Sathiyadhas, Martin Britto Dhas Sathiyadhas Amalapushpam, Muthuvel Vijaya, Raju Suresh Kumar, Abdulrahman I. Almansour, Acoustic shock wave recovery experiments on cubic zinc sulfide nanoparticles for electrical and magnetic switches applications, Ceramics International, 2024, 50,7418-7430, https://doi.org/10.1016/j.ceramint.2023.12.028

[16] S. Oviya, F. Irine Maria Bincy, S.A. Martin Britto Dhas, Raju Suresh Kumar, P. Kannappan, Ikhyun Kim, Tuning the band gap of bismuth sulfide via acoustic shock waves to harness the full visible spectrum for enhanced solar cell applications, Materials Chemistry and Physics, 2025, 333, 130287. https://doi.org/10.1016/j.matchemphys.2024.130287

[17] Yoga Indra Eniya Raveendran, Vijaykumar Krishnan, Martin Britto Dhas Sathiyadhas Amalapushpam, and Vigneashwari Balasubramanian, Investigation of hawleyite-type cadmium sulfide under the influence of acoustic shockwaves, Z. Phys. Chem. 2025. https://doi.org/10.1515/zpch-2025-0101

[18] Boping Yang, Junjie Cang, Zhiling Li, Jian Chen, Nanocrystals as performance-boosting materials for solar cells, Nanoscale Adv., 2024, 6, 1331. https://doi.org/10.1039/D3NA01063E

[19] A. Grzechnik, K. Friese, Pressure-induced orthorhombic structure of PbS, J. Phys. Condens. Matter. 2010, 22, 095402. https://doi.org/10.1088/0953-8984/22/9/095402

[20] P. Bhambhani, N. Munjal, G. Sharma, V. Vyas, B.K. Sharma, First-principles study of B1 to B2 phase transition in PbS, J. Phys. Conf. 2012, 377. https://doi.org/10.1088/1742-6596/377/1/012068

[21] S.J. Heo, S. Yoon, S.H. Oh, D.H. Yoon, H.J. Kim, Influence of high-pressure treatment on charge carrier transport in PbS colloidal quantum dot solids, Nanoscale. 2014, 6, 903-907. https://doi.org/10.1088/1742-6596/377/1/012068

[22] H. Zhang, G. Zhang, J. Wang et al., Structural and electrical transport properties of PbS quantum dots under high pressure, Journal of Alloys and Compounds, 2021, 857, 157482, https://doi.org/10.1016/j.jallcom.2020.157482

[23] Kim, K., Sakthivel, S., Sahadevan, J., Sivaprakash, P., & Kim, I. Effect of Shock Wave Exposure on Structural, Optical and Magnetic Properties of Lead Sulfide Nanoparticles, Journal of the Korean Society of Visualization, 2024, 22(1), 18-27.

[24] Oviya, S., Bincy, F. I. M., Kumar, R. S., Kannappan, P., Kim, I., & Dhas, S. A. M. B, Optimising the photocatalytic degradation efficiency of bismuth sulphide: widening visible light absorption via acoustic shock wave exposure. Materials Research Innovations, 2025, 29(6), 411-422. https://doi.org/10.1080/14328917.2025.2478410

[25] Oviya Sekar, F. Irine Maria Bincy, Raju Suresh Kumar, Kannappan Perumal, Ikhyun Kim and S. A. Martin Britto Dhas, Reversible phase transition and tunable band gap in zinc telluride induced by acoustic shock exposure, Dalton Trans., 2025,54, 3188-3206. https://doi.org/10.1039/D4DT03393K

[26] Oviya Sekar, F. Irine Maria Bincy, Ikhyun Kim, and S.A. Martin Britto Dhas, Acoustic shock-Engineered CaO Nanoparticles from Egg shells: Dual enhancement of Photocatalytic and Anitbacterialproperties, Chemistry Select, 10 (41), 2025. https://doi.org/10.1002/slct.202503601

[27] H.S. Aziz, S. Rasheed, R.A. Khan, A. Rahim, J. Nisar, S.M. Shah, F. Iqbal, A.R. Khan. Evaluation of electrical, dielectric and magnetic characteristics of Al-La doped nickel spinel ferrites, RSC Adv. 2016, 6,6589. https://doi.org/10.1039/C5RA20981A

[28] T J B Holland and S A T Redfern,Unit cell refinement from powder diffraction data: the use of regression diagnostics. Mineralogical Magazine 61: 65-77 (1997). https://doi.org/10.1180/minmag.1997.061.404.07

[29] Z. Su, W. L. Shaw, Y. R. Miao, S. You, D. D. Dlott and K. S, Shock Wave Chemistry in a Metal-Organic Framework, J. Am. Chem. Soc., 2017, 139, 4619-4622. https://doi.org/10.1021/jacs.6b12956

[30] M. El-Hagary, S.H. Moustafa, M.I. Amer, G.M.A. Gad, M. Emam-Ismail, H. Hashem, Linear, non-linear optical properties and magnetic studies of spray pyrolysis nanocrystalline $Sn_{1-x}Co_xO_2$ films for multifunctional optoelectronic and spintronic applications, J. Mater. Res. Technol. 2021, 13, 2310-2324. https://doi.org/10.1016/j.jmrt.2021.05.111

[31] F. Irine Maria Bincy, S. Oviya, Raju Suresh Kumar, P. Kannappan, S. Arumugam, Ikhyun Kim & S. A. Martin Britto Dhas (21 Oct 2024): Investigation of bismuth selenide's structural stability and tunable bandgap under exposure to acoustic shock waves for solar cell and aerospace applications, Mechanics of Advanced Materials and Structures.

[32] Nasiri-Tabirizi B. Thermal treatment effect on structural features of mechano-synthesized fluorapatite-titania nanocomposite: A comparative study. J.Adv.Ceram., 2014, 3:31-42. https://doi.org/10.1007/s40145-014-0090-4

[33] M. Ezzeldien, F.Gami, Z.A.Alrowaili, E.R.Shaaban, M.El-Hagary, The influential role of ITO heat treatment on improving the performance of solar cell n-ITO/p-Si junction: Structural, optical, and electrical characterizations, Mater. Today. Commun. 2022, 30, 103272. https://doi.org/10.1016/j.mtcomm.2022.103272

[34] T. Roisnel, J.R. Carvajal, Win PLOTR, a window tool for powder diffraction pattern analysis, Mater. Sci. Forum 378-381 (2001) 118-123. https://doi.org/10.4028/www.scientific.net/MSF.378-381.118

[35] A. Bohre, O.P. Shrivastava, K. Avasthi, Solid state synthesis and structural refinement of polycrystalline phases: $Ca_{1-2x}Zr_4M_{2x}P_{6-2x}O_{24}$ (M=Mo, x = 0.1 and 0.3), Arabian J. Chem. 2016, 9, 736-744. https://doi.org/10.1016/j.arabjc.2013.04.008

[36] Haiwa Zhang, Guozhao Zhang, Jia Wang, Qinglin Wang, Hongyang Zhu, Cailong Liu, Structural and electrical transport properties of PbS quantum dots under high pressure, Journal of Alloys and Compounds, 2021, 857, 15, 157482. https://doi.org/10.1016/j.jallcom.2020.157482

[37] Lijing Yu, Pin Tian, Libin Tang, Qun Hao, Kar Seng Teng, Hefu Zhong, Biao Yue, Haipeng Wang, Shunying Yan, Fast-Response Photodetector Based on Hybrid Bi_2Te_3/PbS Colloidal Quantum Dots. Nanomaterials 2022, 12, 3212. https://doi.org/10.3390/nano12183212

[38] Chao Liu, Yang Jiang, Jian Huang, and Hongyan Duan, Facile synthesis of colloidal PbS quantum dots, International Journal of Nanoscience, 2012, 11(6), 1240041. https://doi.org/10.1142/S0219581X12400418

[39] Nayely Torres-Gomez, Diana F. Garcia-Gutierrez, Alan R. Lara-Canche, Lizbeth Triana-Cruz, Jesus A. Arizpe-Zapata , Domingo I. Garcia-Gutierrez, Absorption and emission in the visible range by ultra-small PbS quantum dots in the strong quantum confinement regime with S-terminated surfaces capped with diphenylphosphine, Journal of Alloys and Compounds, 2021, 860, 158443. https://doi.org/10.1016/j.jallcom.2020.158443

[40] Shkir, M., Chandekar, K.V., Alshahrani, T., et al. A novel terbium doping effect on physical properties of lead sulfide nanostructures: A facile synthesis and characterization. Journal of Materials Research 35, 2664-2675 (2020). https://doi.org/10.1557/jmr.2020.216

[41] Sajid Ahmad, Ajay Singh, Shovit Bhattacharya, Rantita Basu, Ranu Bhatt, Anil Bohra, K.P. Muthe, S.C. Gadkari, Lead sulphide: Low cost, abundant thermoelectrics, AIP Conf. Proc. 2018, 1942, 110013. https://doi.org/10.1063/1.5028996

[42] Sivakumar Aswathappa, Lidong Dai, S. Sahaya Jude Dhas, S. A. Martin Britto Dhas, Eniya Palaniyasan, Raju Suresh Kumar, and Abdulrahman I. Almansour, Cryst. Growth Des. 2024, 24, 491−498. https://doi.org/10.1021/acs.cgd.3c01180

[43] Sixberth Mlowe, Ginena B. Shombe, Matthew P. Akerman, Egid B. Mubofu, Paul O'Brien, Philani Mashazi, Tebello Nyokong, Neerish Revaprasadu, Morphological influence of deposition routes on lead sulfide thin films, Inorganica Chimica Acta, 2019, Volume 498, 119116, ISSN 0020-1693. https://doi.org/10.1016/j.ica.2019.119116

[44] S. Oviya, F. Irine Maria Bincy, S. Arumugam, K. Kamala Bharathi, Raju Suresh Kumar, P.Kannappan, Ikhyun Kim and S. A. Martin Britto Dhas, Acoustic shock wave-induced phase transition in indium selenide: tuning band gap energy for solar cell applications, Cryst Eng Comm, 2024, 26, 2498-2509. https://doi.org/10.1039/D4CE00012A

[45] P.S. Khiew, S. Radiman, N.M. Huang, Md. Soot Ahmad, Studies on the growth and characterization of CdS and PbS nanoparticles using sugar-ester nonionic water-in-oil microemulsion, J. Cryst. Growth, 2003, 254, 235-243. https://doi.org/10.1016/S0022-0248(03)01175-8

[46] Yu Zhao, Xue-Hong Liao, et al., Synthesis of lead sulfide nanocrystals via microwave and sonochemical methods, Mater. Chem. Phys. 87 (2004) 149-153. https://doi.org/10.1016/j.matchemphys.2004.05.026

[47] Zamin Q. Mamiyev, Narmina O. Balayeva, Preparation and optical studies of PbS nanoparticles, Optical Materials, 2015, Volume 46, Pages 522-525. https://doi.org/10.1016/j.optmat.2015.05.017

[48] L.E. Brus, Electron-electron and electron-hole interactions in small semiconductor crystallites: The size dependence of the lowest excited electronic state, J. Chem. Phys. (1984), 80, 4403-4409. https://doi.org/10.1063/1.447218

[49] R. Palomino Merino, O. Portillo Moreno, J.C. Flores Gracia, J. Hernandez Tecorralco, J. Martinez Juarez, A. Moran Torres, E. Rubio Rosas, G. Hernandez Tellez, R. Gutierrez, L.A. Chaltel Lima, PbS nanostructured thin films by in situ Cu-doping, J. Nanoci. Nanotechnol. 2014, 14, 5408-5414. https://doi.org/10.1166/jnn.2014.8664

[50] J.I. Pankove, Optical processes in semiconductors, Prentice Holl, New Jersy, 1971.

[51] E.H.H. Hasabeldaim, H.C. Swart, and R.E. Kroon, “Luminescence and stability of Tb dopedCaF2 nanoparticles”, RSC Adv.13, 2023, 5353-5366. https://doi.org/10.1039/D2RA07897J

[52] Jung-Hsuan Chen, Cheun-Guang Chao, Jong -Chyan Ou, Tzeng-Feng Liu, Growth and characteristics of lead sulfide nanocrystals produced by the porous alumina membrane, Surface Science, 601, 2007, 5142-5147. https://doi.org/10.1016/j.susc.2007.04.228

[53] A.K. Mishra, S. Saha, Synthesis and characterization of PbS nanostructures to compare with bulk, Chalcogenide Letters, Vol.17 (3), 2020, 147-159. https://doi.org/10.15251/CL.2020.173.147

[54] Jing X, Zhou D, Sun R, Zhang Y, Li Y, Li X, Li Q, Song H, Liu B, Enhanced photoluminescence and photo responsiveness of Eu^{3+} ions doped $CsPbCl_3$ perovskite quantum dots under high pressure. Adv. Funct. Mater. 31, 2021, 2100930-2100940. https://doi.org/10.1002/adfm.202100930

[55] S. A. M. Lima, F. A. Sigoli, M. Jafelicci, and M. R. Davolos, Luminescent properties and lattice defects correlation on zinc oxide, Int. J. Inorg. Mater. 2001. 3, 749. https://doi.org/10.1016/S1466-6049(01)00055-1

[56] S. V. M. Pavana, C. Karthik, R. Ubic, M. S. Ramachandra Rao, and C. Sudakar. Tunable bandgap in $BiFeO_3$ nanoparticles: The role of microstrain and oxygen defects, Appl. Phys. Lett. 2013, 103, 022910. https://doi.org/10.1063/1.4813539

[57] R. Udayabhaskar, B. Karthikeyan, Role of micro-strain and defects on band-gap, fluorescence in near white light emitting Sr doped ZnO nanorods, Appl. Phys. 2014, 116, 094310. https://doi.org/10.1063/1.4893562
